ADVANCED FUNCTIONAL MATERIALS
www.afm-journal.de

# 3D-Printed and Recombinant Spider Silk Particle Reinforced Collagen Composite Scaffolds for Soft Tissue Engineering

*Kim Sarah Koeck, Vanessa Tanja Trossmann, and Thomas Scheibel**

**Collagen is one main component of the extracellular matrix (ECM) in natural tissues and is, therefore, well suited as a biomaterial for tissue engineering. In this study, a method is presented to 3D-bioprint collagen into a precipitation bath comprising recombinantly produced spider silk protein eADF4(C16) yielding a composite with excellent mechanical properties. The spider silk precipitation bath induced assembly of the collagen into fibrils, and subsequent addition of potassium phosphate buffer lead to the formation of silk particles and stabilization of the collagen fibrils. The produced collagen-silk composite scaffolds show an internal structure of homogeneously distributed and interacting collagen fibrils and spider silk particles with significantly better mechanical properties compared to plain collagen scaffolds. Further, enzymatic degradation assays of the scaffolds over a 7-day period show higher stability of the collagen-silk scaffolds compared to plain collagen scaffolds in the presence of wound proteases. Using the spider silk variant eADF4(C16-RGD) further increases compressive stress and elastic modulus compared to that of the unmodified variant. Finally, it is shown that the unique collagen-spider silk composite scaffolds comprising the cell-binding domains of collagen and the RGD sequence in the spider silk variant represent a promising material for soft tissue regeneration.**

## 1. Introduction

Type I collagen is the predominant extracellular matrix (ECM) protein in the body. It transfers load in tissues and provides cells a highly biocompatible environment. Its mechanical and biological properties make collagen a suitable material for implantable medical scaffolds as well as for 3D bioprinting. However, current inks for bioprinting containing plain collagen have several shortcomings, such as poor printability and often weak mechanical properties after printing compared to polymer-based gels. Most collagen-based inks have been developed from aqueous, acidic collagen solutions at concentrations below 5 mg $mL^{-1}$.[1] They are not suitable for direct bioprinting without additional stabilization by chemical cross-linking. Direct 3D-printing was only possible and successful for highly concentrated acidic collagen solutions, which show high viscosities and shear thinning behavior.[2] Rhee et al. showed that collagen concentrations of 13, 15, and 18 mg $mL^{-1}$ exhibited significantly higher shape fidelity than lower concentrated solutions.[3] The printed constructs exhibited low mechanical properties and required an environment inducing fibrillization and cross-linking of the collagens.[2] Such cross-linking can be achieved at physiological conditions (neutral pH and 37 °C), where collagens start to self-organize time-dependently into fibrils. Unfortunately, direct 3D-printing of already self-assembled collagen hydrogels is not possible due to needle clogging and phase separation of the ink. High shear forces arise due to the high pressure of 1–2 bar, leading to the separation of an aqueous and the solid fibrillar phase. This drawback substantially hampers direct 3D-bioprinting of assembled collagen.

In order to produce scaffolds with feasible mechanical properties, printed collagen scaffolds have been additionally treated using chemical cross-linking agents to obtain covalent bonds, including glutaraldehyde, 1-ethyl-3-(−3-dimethylaminopropyl) carbodiimide hydro-chloride/N-Hydroxy-sulfosuccinimid, genipin, Irgacure, lithium-Phenyl-2,4,6-trimethylbenzoylphosphinat, ruthenium, formaldehyde, epoxy-functional cross-linking agent, or combinations thereof.[4] However, such cross-linking agents are usually cytotoxic and must be thoroughly removed before the scaffolds can be used with living cells or as implants.[5,6] Delgado et al. explored the response of host tissue and macrophages to different cross-linking methods for stabilizing

K. S. Koeck, V. T. Trossmann, T. Scheibel
Department of Biomaterials
University of Bayreuth
Prof.-Rüdiger-Bormann Str. 1, 95447 Bayreuth, Germany
E-mail: thomas.scheibel@uni-bayreuth.de
T. Scheibel
Bayreuther Zentrum für Kolloide und Grenzflächen (BZKG)
Bayreuther Zentrum für Molekulare Biowissenschaften (BZMB)
Bayreuther Materialzentrum (BayMAT)
Bayerisches Polymerinstitut (BPI)
University of Bayreuth
Universitätsstraße 30, 95447 Bayreuth, Germany
T. Scheibel
Faculty of Medicine
University of Würzburg
Pleicherwall 2, 97070 Würzburg, Germany

The ORCID identification number(s) for the author(s) of this article can be found under https://doi.org/10.1002/adfm.202407760



**DOI: 10.1002/adfm.202407760**

collagen-based scaffolds. In vitro and in vivo data showed that chemical cross-linking methods altered the physiological wound-healing process, even at low concentrations. Importantly, high cross-linking densities were associated with an enhanced macrophage response, reduced cell infiltration, increased expression of proinflammatory cytokines, delayed wound healing, and chronic wounds.[6]

Another widely used approach to improve the physicochemical properties of collagen constructs is blending the collagen solution with other natural biopolymers to form interpenetrating networks, including silk fibroin,[7] chitosan,[8] alginate,[9] or hyaluronic acid (HA).[10] However, even with this approach additional cross-linking using toxic substances is still necessary in most cases to obtain mechanically stable constructs. Pei et al. produced a printable ink by mixing individually homogenized collagen and HA in an acetic acid solution. In order to improve mechanical properties, the printed scaffold was further cross-linked.[11]

To obtain collagen scaffolds with improved mechanical properties, also particle reinforcement has been employed, which relies on introducing synthetic polymers or mineral fillers to yield composite materials. Hydroxyapatite–collagen scaffolds are most commonly prepared by freeze-drying a suspension of collagen fibrils and Hydroxyapatite particles,[12] compression molding,[13] or precipitating Hydroxyapatite within a freeze-dried collagen scaffold.[14] However, these methods still require cross-linking of the collagen matrix, and the mixtures are not 3D-printable.

Finally, viscoelastic,[15] or thermoreversible[16,17] supporting baths composed of a microparticle slurry, or an isotonic solution bath[18] providing support during printing, which could subsequently be removed upon melting at 37 °C, have been used to obtain 3D-printed collagen scaffolds at a good resolution. Some commercially available collagen inks (bioinks Lifeink 240 or Lifeink 200, 30–45 mg $mL^{-1}$ collagen, Sigma–Aldrich) can be printed in a stabilization bath containing gelatin, alginate, or agarose particles. However, the acidic pH of the collagen bioinks is not suitable for adding cells before printing, and cells can only be seeded onto the printed scaffold afterward. Additionally, no evaluation of the mechanical properties was performed.[16]

In this study, 3D-bioprinting of a concentrated collagen solution (15 mg $mL^{-1}$) into a pH-neutral aqueous precipitation bath consisting of 20 mg $mL^{-1}$ recombinant spider silk eADF4(C16) with or without the RGD motif in Tris buffer (pH 7.5) was performed to overcome the limitations mentioned above. Spider silk materials are interesting for biomedical applications and tissue engineering due to their unique intrinsic properties, such as slow biodegradability,[19] excellent biocompatibility,[19,20] low immunogenicity,[21] and microbial resistance.[22–32] For instance, several studies have demonstrated that spider silk materials exhibit excellent in vivo biocompatibility and appropriate biodegradation without causing an immune or foreign body response making them suitable for wound healing and tissue engineering applications.[19–21,33–40] In addition, genetic engineering and recombinant production enable the generation of customized and application-specific spider silk proteins exhibiting the desired modifications and functions.[31,32,41–44] A further exceptional benefit of silk proteins is their ability to be processed in a magnitude of morphologies including films,[20,32–34,39,45] capsules,[33,46] membranes,[35,38,47] particles,[48,49] foams,[50] hydrogels,[19,51] fibers,[21,36,37,52] allowing application in various fields.[31,32,40,44,53]

It is a known fact that blending different natural or synthetic polymers as raw materials or in processed morphologies allow the generation of tailor-made, adjustable composite materials combining the beneficial properties and overcoming the individual limitations of the single components.[31,54] Thus, possible reasons for blending spider silk with other polymers are increasing/adopting the mechanical properties and/or bioactivity of the resulting scaffold, optimizing the biodegradability as well as cost reduction.[31,55] For instance, composite films made of recombinant spider silk and collagen showed enhanced mechanical properties and cell interaction in comparison to pure spider silk films.[56] Furthermore, composite scaffolds made of a collagen type I hydrogel and native spider silk fibers (*Trichonephila clavipes*) enhanced the differentiation of adipose-derived stromal cells for tendon tissue engineering.[57]

Here, collagen fibril formation of an acidic collagen I/III solution occurred upon contact with the spider silk precipitation bath due to pH increase from 3.0 to 7.5. This precipitation occurred in a suitable time range that allowed a layer-by-layer deposition of the collagen ink in order to form a stable 3D-construct with high shape fidelity. Subsequent addition of 1 M potassium phosphate (KPi, pH 8.0) induced spider silk particle formation, strengthened fibril formation and resulted in mechanically stable particle-reinforced scaffolds. Using the RGD-containing spider silk variant within the precipitation bath resulted in a scaffold showing superior mechanical properties compared to ones using the unmodified eADF4(C16) silk variant. The resulting collagen-spider silk composite scaffolds are biocompatible, biodegradable, bioactive, and promising for tissue engineering applications.

## 2. Results and Discussion

Rheological measurements revealed viscoelastic properties and shear-thinning behavior of the acidic collagen I/III ink (Figure S1, Supporting Information) making it perfectly suitable for extrusion-based bioprinting. However, direct deposition of filaments in a layer-by-layer manner was not possible on a dry surface without collapsing. On the one hand, there was no evaporation of the solvent to solidify the printed collagen filaments. On the other hand, no pH-increase happened to induce fibrilization of the collagen molecules. Indeed, the addition of a pH-neutral coagulation bath increased the collagen fibril formation, but the extruded filaments still displayed too low mechanical properties to enable a continuous layer-by-layer deposition without collapsing (Figure S2A, Supporting Information). To overcome these limitations, we added recombinant spider silk proteins as biological stabilizers to the printing process yielding in mechanically stable composite scaffolds (Figure S2B,C, Supporting Information). The preparation of collagen-eADF4(C16)-composite scaffolds required a two-step assembly process (**Figure 1**). In the printing process, a 15 mg $mL^{-1}$ collagen solution was extruded into a precipitation bath of aqueous eADF4(C16) or eADF4(C16-RGD) spider silk solution at a concentration of 20 mg $mL^{-1}$ (Figure 1D). First, the extrusion of acidic collagen solution into the eADF4(C16) precipitation bath at physiological pH (pH 7.5) resulted in fibril formation of the collagen molecules. Second, the assembly of the spider silk proteins into particles was induced by

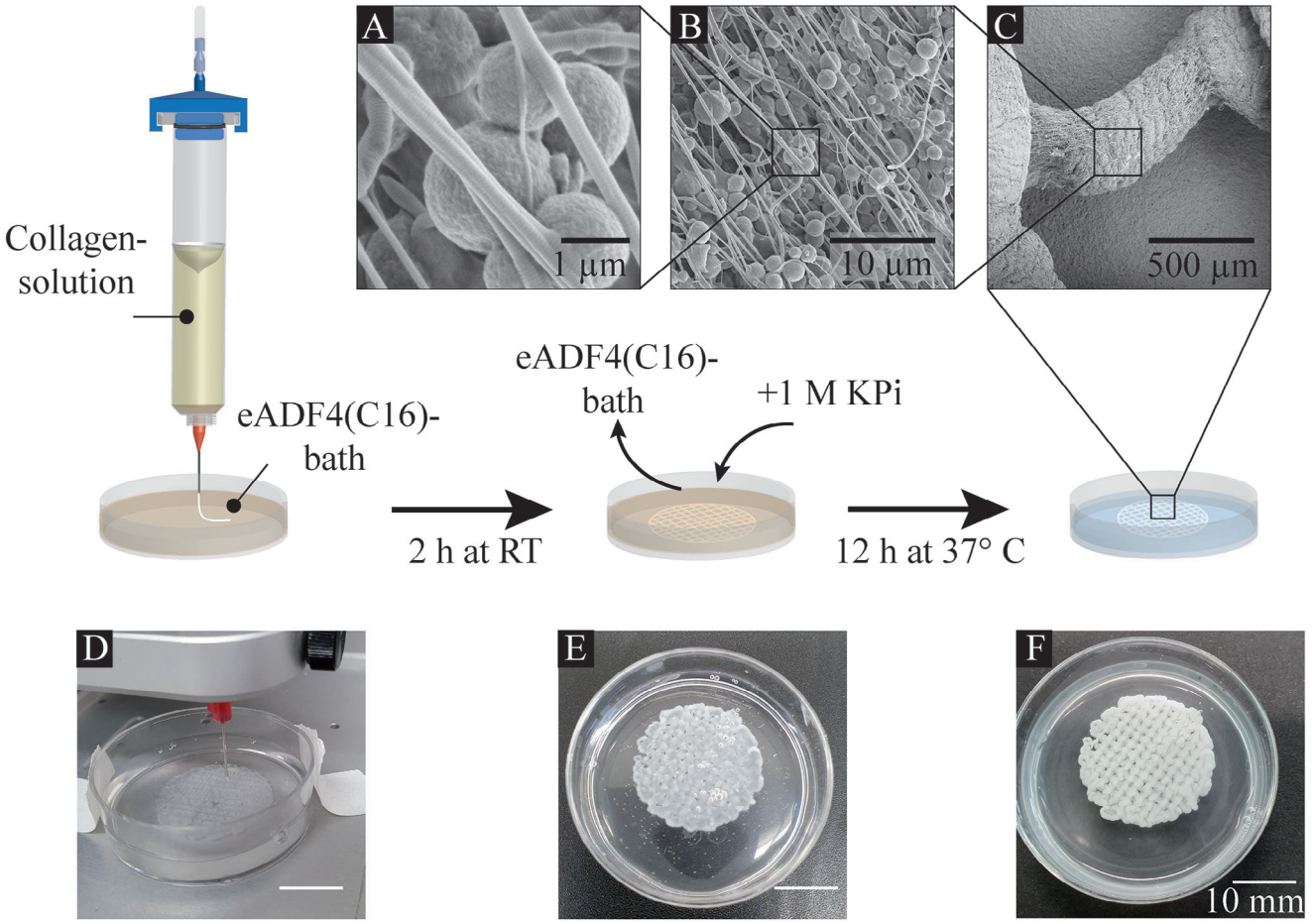


**Figure 1.** Schematic representation of the 3D-printing process of collagen-eADF4(C16)-scaffolds by extrusion of 15 mg $mL^{-1}$ collagen into a 20 mg $mL^{-1}$ spider silk precipitation bath. After an incubation period of 2 h at RT, the excess silk solution was removed, and silk particle formation was induced by adding 1 M KPi. SEM analysis showed the structure of the scaffolds consisting of collagen fibrils and spider silk particles (A–C). Macroscopic images of the scaffolds (D) during the printing process, (E) after incubation in the silk precipitation bath, and (F) after incubation in 1 M KPi at 37 °C overnight. Scale bars in D–F: 10 mm.

post-treatment of the scaffolds with 1 M KPi (pH 8.0).[52] Due to the collagen fibril formation, the precipitation bath allowed the collagen solution to be printed layer-by-layer with a firm and uniform connection of individual layers. After printing, the scaffolds were left in the spider silk solution for 2 h at RT. The pH of the spider silk solution resulted in crosslinking and fibril formation of the collagen filaments, recognizable by a turbidity change from transparent to a more whitish color (Figure 1E). However, in this process, spider silk molecules were also intercalated between the collagen fibrils. Subsequently, the excess spider silk solution was removed, and the scaffolds were post-treated by adding 1 M KPi at 37 °C overnight. The post-treatment led to the formation of spider silk particles,[53] indicated by the white color, and thus, to the formation of stable collagen-silk composite structures (Figure 1F), which could be confirmed by SEM (Figure 1A–C; Figure S2D,E, Supporting Information).

To analyze the effect of the spider silk proteins on collagen I/III assembly and precipitation in more detail, the collagen solution was manually extruded in 10 mg $mL^{-1}$ aqueous recombinant spider silk solution made of eADF4(C16) or Tris buffer (pH 7.5) without protein.[60] Compared to Tris buffer, the spider silk protein solution supported collagen precipitation indicated by a faster turbidity change from transparent to a whitish color (Figure S2A–C, Supporting Information). Furthermore, the subsequent addition of KPi led to spider silk particle formation and stabilization of the extruded collagen indicated by mechanically stable, white strands (data not shown). A single-layer square with 20 × 20 mm and a strut spacing of 1.35 mm was printed into a precipitation bath consisting of rhodamine-labeled eADF4(C16) solutions to investigate, if spider silk is only assembled in particles or also incorporated in the collagen fibrils. Therefore, 15 mg $mL^{-1}$ collagen solution was printed into spider silk precipitation baths (20 mg $mL^{-1}$) either containing 100% (v/v) unlabeled (**Figure 2A**), 90% (v/v) unlabeled and 10% (v/v) Rhodamine-labeled (Figure 2B) or 100% (v/v) Rhodamine-labeled (Figure 2C) eADF4(C16). Using light and fluorescence microscopy, the two different morphologies of the proteins, namely fibrils and particles, could be visualized (Figure 2D–F). The fluorescently labeled samples showed red eADF4(C16) particles and unlabeled collagen fibrils connecting the silk particles (Figure 2E,F). Thus, the increase of pH led to collagen fibril formation, while spider silk particles were

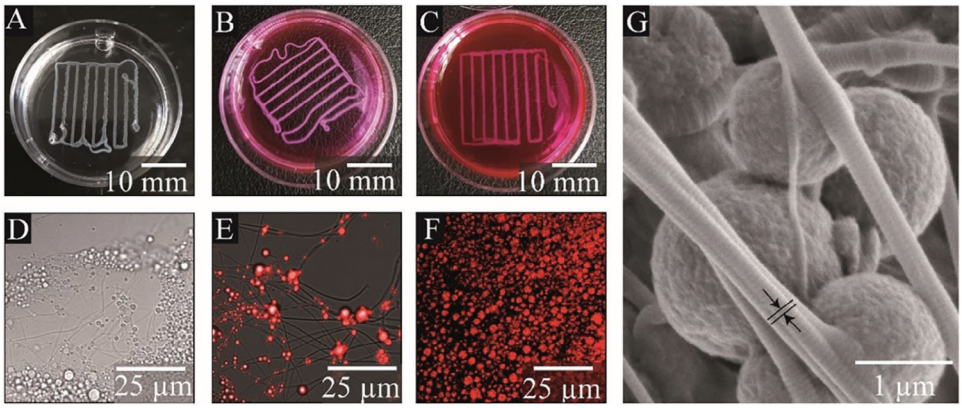


**Figure 2.** Examination of collagen filaments printed in 20 mg mL$^{-1}$ unlabeled (A,D), 10% (B,E), and 100% (C,F) rhodamine-labeled eADF4(C16) solution. (G) SEM of the collagen-silk-composite showing the highly repetitive D-band pattern (black arrows indicate the 67 nm band) typical for native collagen fibrils and spider silk particles.

precipitated using potassium phosphate. The particle-reinforced, fibrillar microstructure of the filaments was further analyzed using SEM after dehydration (Figure 2G). On the one hand, it could be seen that the collagen fibrils exhibited the unique, periodic D-band pattern of collagens.[61] On the other hand, the spider silk particles showed the already known slightly rough surface topography.[58,59]

To determine the optimal precipitation bath concentration, the 15 mg mL$^{-1}$ collagen solution was printed into 20, 30, 40, and 50 mg mL$^{-1}$ eADF4(C16) solutions (**Figure 3**). As a control, collagen was printed into pure Tris buffer (pH 7.5, data not shown). Printing of the collagen solution in eADF4(C16) precipitation baths showed uniform filaments at all concentrations. The resulting filaments precipitated slowly in the eADF4(C16) solutions, changing the color of the collagen filament within 40–60 s from transparent to turbid. After incubation in the silk solutions and subsequent precipitation of spider silk particles using KPi, clear demarcations between the collagen filaments were visible at eADF4(C16) concentrations of 20 and 30 mg mL$^{-1}$ (Figure 3A,B). At higher spider silk concentrations (40 and 50 mg mL$^{-1}$), the eADF4(C16) solution settled around the collagen filaments like a film (Figure 3C,D). That film formation resulted from spider silk self-assembly.

It is known that recombinant eADF4(C16)-based proteins could self-assemble from unstructured monomers into $\beta$-sheet-rich nano-fibrils by structural rearrangement over time,[59,62] and the fibril formation kinetics are influenced by the protein concentration and the temperature. Furthermore, at sufficient protein concentrations, interconnected and physically crosslinked, nanofibrillar hydrogels could be formed.[62] With increasing protein concentration, the fibril formation accelerated, and physically crosslinked hydrogels were formed, which could not be removed completely after the 2 h incubation period. In that cases, besides eADF4(C16) particles also nanofibrils were formed. Since the hydrogel formation has also already been started in the 30 mg mL$^{-1}$ precipitation bath, the printed collagen filaments could only be removed individually from the surroundings and handled easily in case of the 20 mg mL$^{-1}$ eADF4(C16) solution. In contrast, samples printed in Tris buffer were too unstable to be removed.

In order to develop a self-assembly model of collagen fibrils and spider silk particles, time-dependent turbidity measurements and SEM measurements of the resulting scaffolds were conducted (**Figure 4**). In this context, eADF4(C16)-RGD was used with regard to the future tissue engineering application of the collagen-silk-scaffolds.

The turbidity measurements showed that self-assembly and fibril formation of collagen started immediately after the addition of the spider silk solutions or Tris buffer (Figure 4A+B). The turbidity of the Coll-Tris samples was more or less similar during the 120 min incubation time indicating a slow self-assembly into collagen triple-helices without twists and entanglements. In contrast, turbidities induced by eADF4(C16) or eADF4(C16-RGD) solutions continuously increased up to minute 120 indicating beneficial, additional conformational changes, restructuring, and entanglements induced by silk molecules. The addition of KPi (pH 8.0) increased the turbidity of all three samples significantly (Figure 4A). These similar curve progressions indicated the precipitation of unassembled collagen and spider silk molecules. However, the precipitation of recombinant spider silk particles increased the apparent turbidity further. In contrast, samples incubated without KPi displayed an even curve progression and constant increase in turbidity indicating continuous protein self-assembly (Figure 4B).

Afterward, the samples were gradually dehydrated through an alcohol series, freeze-dried, and the morphology was examined using SEM (Figure 4C+D). Figure 4D shows the samples without additional KPi. Collagen fibrils were visible in all samples. The diameters of the collagen fibrils were ≈200 nm within the SEM images determined using Image J software. However, additional eADF4(C16)- and eADF4(C16-RGD)-assemblies were detectable between the collagen fibrils (Figure 4D, white arrows) leading to twists, entanglements, and interconnections responsible for the turbitiy increase of spider silk-containing samples. The addition of KPi resulted in the formation of eADF4(C16) and eADF4(C16-RGD) particles by salting out (Figure 4C). The diameter of the resulting spider silk particles ranged ≈1,3 µm. In general, collagen was able to self-assemble into nanofibrils in Tris buffer in the presence and absence of KPi. However, the self-assembly was not finished after 120 min leading to increased aggregation of

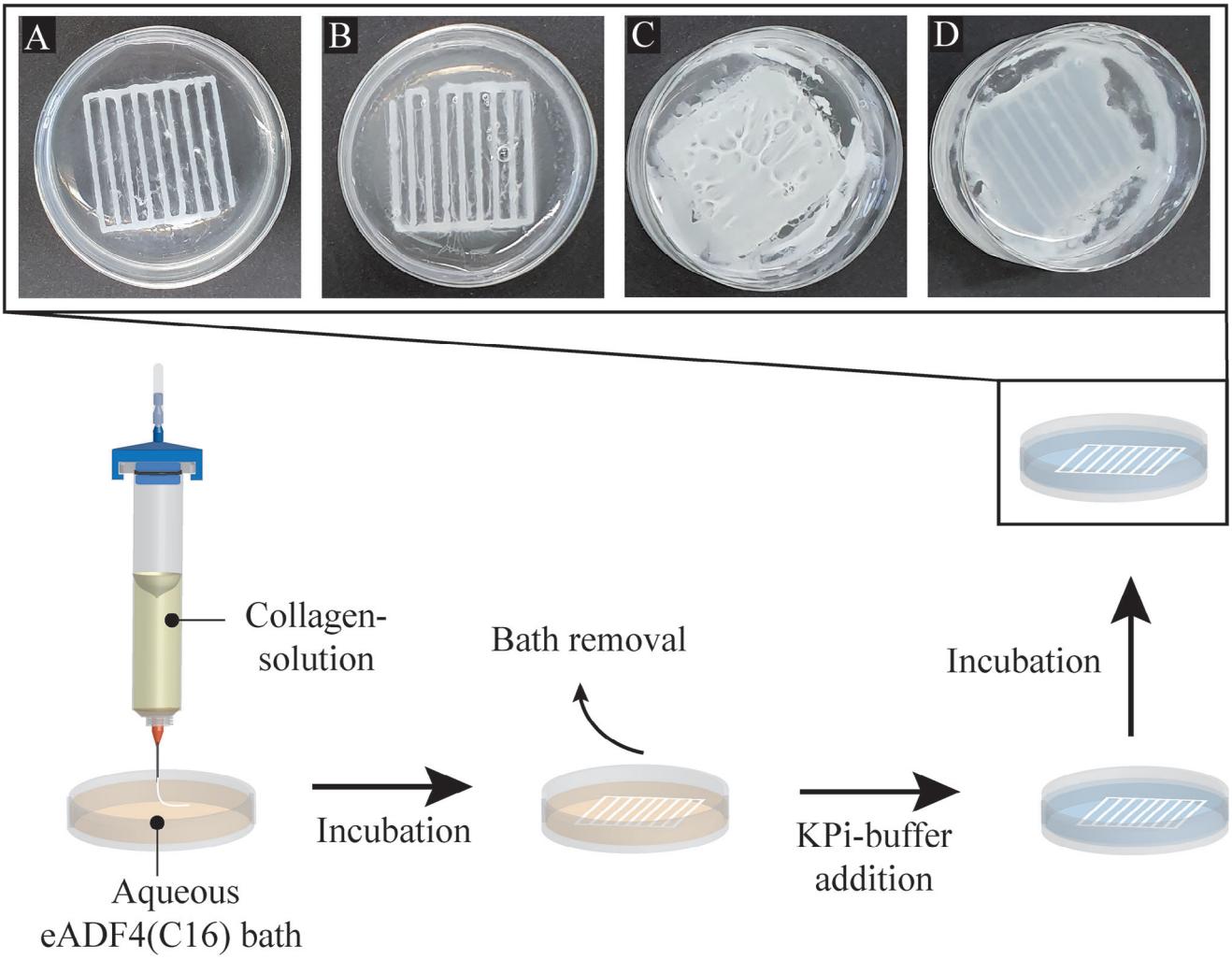


**Figure 3.** Effect of the eADF4(C16) bath concentration, namely (A) 20 mg mL$^{-1}$, (B) 30 mg mL$^{-1}$, (C) 40 mg mL$^{-1}$, and (D) 50 mg mL$^{-1}$ eADF4(C16) in Tris buffer (pH 7.5), on the collagen-silk-scaffold formation after 3D-printing and addition of 1 M potassium phosphate (KPi) ($n = 3$).

unassembled collagen after addition of KPi. In addition to single collagen fibrils, many aggregated, melted sheets were visible (Figure 4C, white stars) explaining the significant raise of turbidity.

Based on the turbidity and SEM results, we sketched collagen assembly in absence and presence of spider silk in Tris buffer (pH 7.5) and upon addition of KPi buffer. The resulting structures are influenced by the pH-driven collagen assembly as well as the conformational restructuring and entanglement of collagen and spider silk (Figure 4E).

In order to gain insight into the mechanical properties of the 3D collagen scaffolds, circular scaffolds with a diameter of 10 mm and a height of 1.5 mm were printed in Tris buffer, eADF4(C16) or eADF4(C16-RGD) and subsequently subjected to oscillatory compression tests at RT using a dynamic mechanical analysis (DMA). Stress-compression curves (hysteresis curves) were used to determine the mechanical parameters of compressive stress, compression, and compressive modulus (**Figure 5**). Due to the poorly manageable Coll-Tris scaffolds (Figure S2A, Supporting Information), which collapsed when moved from the dish to the testing device, a mechanical investigation was not possible. Already from this result, it could be deduced that the interaction of the collagen fibrils and the spider silk particles within the 3D scaffolds led to an increase in stability. Scaffolds printed in the eADF4(C16)- or eADF4(C16-RGD)-bath showed good stability and were easy to transfer (Figure S2B,C, Supporting Information). SEM images of the cross-sectional area of a 3D-printed filament of collagen in the eADF4(C16)-bath (Figure S2D,E, Supporting Information) revealed an uniform distribution throughout the construct. While collagen fibrils provided the primary mechanical stability and structural integrity, the silk particles reinforced the fiber network by acting as connection points between the collagen fibrils, increasing the stiffness and strength of the scaffold. Comparing samples printed in eADF4(C16) precipitation bath with and without the RGD sequence it can be clearly seen that the use of eADF4(C16) resulted in lower compressive stresses and compressive moduli in the obtained 3D scaffolds compared to the use of eADF4(C16)-RGD. While the compressive stresses and compressive moduli of the scaffolds printed in eADF4(C16) were 1141 ± 274 kPa and 7628 ± 3069 kPa,

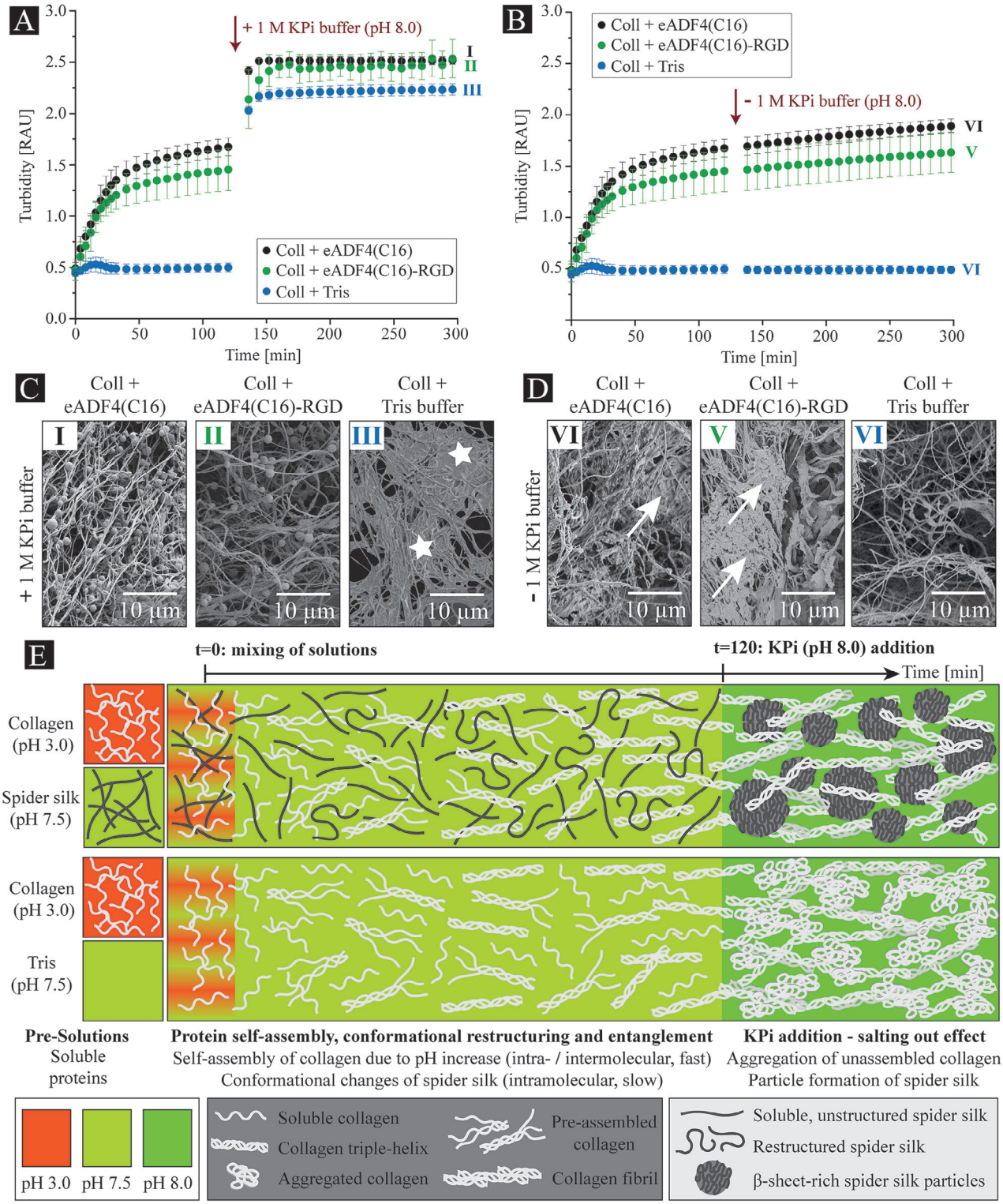


**Figure 4.** Turbidity measurements at 340 nm in relative absorbance units (RAU) for a time period of 300 min to analyze collagen self-assembly behavior in Tris buffer (blue), eADF4(C16) (black) and eADF4(C16-RGD) (green) solution upon addition (A) and absence (B) of 1 M KPi buffer (pH 8.0) after 120 min indicated by brown arrows ($n = 3$). SEM analysis of assembled collagen and Coll-silk structures in presence (C) and absence (D) of KPi buffer. The addition of 1 M KPi after 120 min resulted in particle formation of the spider silk proteins (I + II). White stars designate additional collagen aggregation upon KPi addition (III). In contrast, in the absence of KPi, collagen assembles into regular fibrils (VI), and spider silk also self-assembles over time leading to entanglements and interconnections indicated by white arrows (IV + V). (E) Schematic illustration of the collagen and silk assembly during incubation in Tris buffer (pH 7.5) before and after protein precipitation using 1 M KPi buffer (pH 8.0).

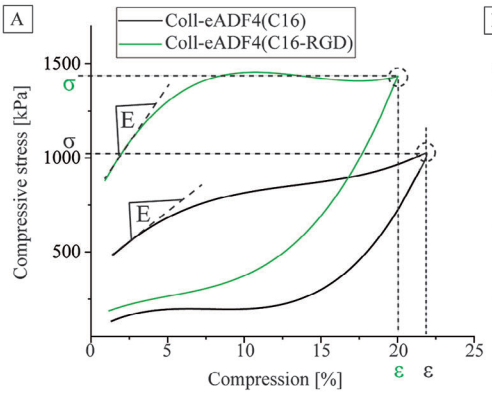


B

| | Coll-eADF4 (C16) | Coll-eADF4 (C16-RGD) |
|---|---|---|
| Crompressive stress σ [kPa] | 1,141 ± 274 | 1,921 ± 1,012 |
| Compression ε [%] | 20 ± 2 | 20 ± 2 |
| Compr. modulus E [kPa] | 7,628 ± 3,069 | 12,311 ± 2,213 |
| Cross section A [mm$^2$] | 86 ± 16 | 75 ± 15 |

**Figure 5.** Mechanical properties of collagen-eADF4(C16) and collagen-eADF4(C16-RGD) scaffolds measured using DMA ($n$ = 8). (A) Representative, fitted compression-compressive stress diagrams of collagen-eADF4(C16) (black) and collagen-eADF4(C16-RGD) (green) scaffolds with plotted compressive stress $\sigma$, compression $\epsilon$ and compression modulus E. (B) Comparison of mechanical properties of collagen-eADF4(C16) and collagen-eADF4(C16-RGD) scaffolds. The specimens were stored in PBS after preparation and measured in the hydrogenated state.

respectively, the scaffolds printed in eADF4(C16)-RGD showed higher values with 1921 ± 1012 kPa and 12311 ± 2213 kPa in comparison. Compression was identical within 20%± 2% in both scaffolds. Figure 5B shows a summary of the mechanical properties of the 3D-printed scaffolds. As previously demonstrated, the additional RGD-peptide increased the mechanical properties and stability of eADF4(C16)-RGD scaffolds.[63] Gao et al. attributed these results to the amino acid arginine and its guanidine side group within the RGD peptide. This side group can interact strongly with other amino acid side groups as well as with itself in a variety of configurations, thereby providing additional cross-linking within the scaffold. Among others, these interactions occur through hydrogen bonds, electrostatic interactions, and salt bridges.[64] These additional cross-linking points can result in a denser network, consequently less water is absorbed into the network leading to an increased stiffness.[65]

To evaluate the stability of the 3D-printed composite scaffolds at wound-like or digestive conditions, in vitro enzymatic degradation was performed over seven days.[66,67] Degradation of Coll-eADF4(C16) and Coll-Tris scaffolds was studied in the presence of proteases (mixture PXIV) of Streptomyces griseus, which resemble digestive conditions, and of collagenases (mixture CHC) of Clostridium histolyticum to simulate wound-like conditions. Scaffolds were entrained in the buffer as a control. Degradation was performed at physiological conditions in an incubator (37 °C, 10% $CO_2$, 95% humidity). **Figure 6** shows the cumulative enzymatic protein degradation and macroscopic images of the samples over a period of 7 days. In the digestive conditions model, a much stronger degradation of the Coll-eADF4(C16) scaffolds was observed compared to the Coll-Tris samples. There was a significant degradation in the Coll-eADF4(C16) sample within the first 3 days, increasing until day 7, while Coll-Tris samples were more stable in the presence of proteases. Here, degradation started only after 6 days and was less pronounced. In contrast, the degradation of Coll-Tris samples in the wound conditions model showed greater degradation, whereas the Coll-eADF4(C16) samples were more stable and showed a slow degradation. Thus, spider silk particles seemed to hinder fast collagen degradation at these

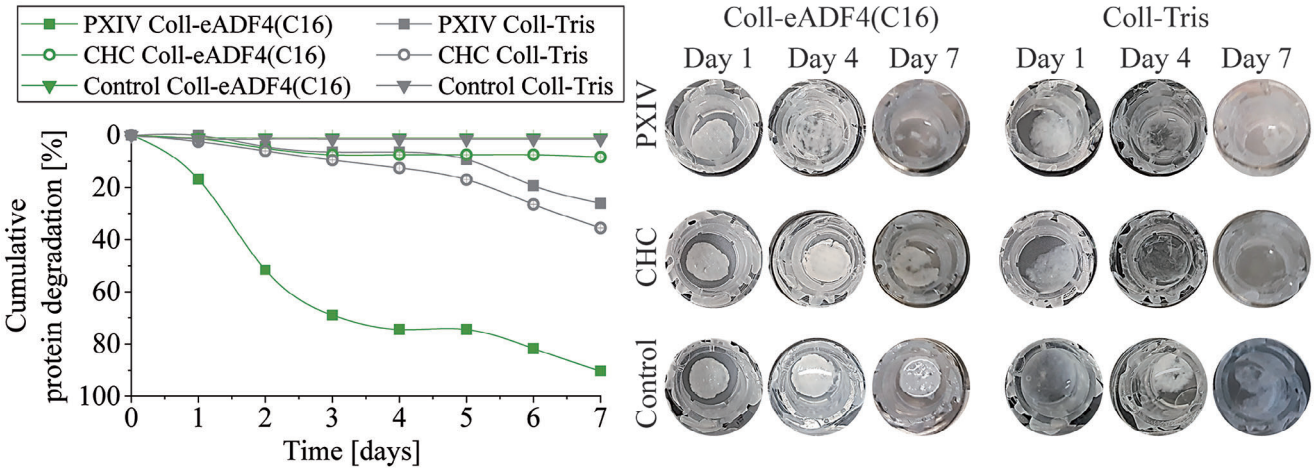


**Figure 6.** Cumulative enzymatic degradation of Coll-eADF4(C16) (green) and Coll-Tris (gray) scaffolds in protease mixture (PXIV, square) as a model for digestive conditions, collagenase mixture (CHC, circle) as a model for wound-like conditions, and buffer control (triangle) over a period of 7 days. Macroscopic images of the digested samples after 1, 4, and 7 days ($n$ = 4).

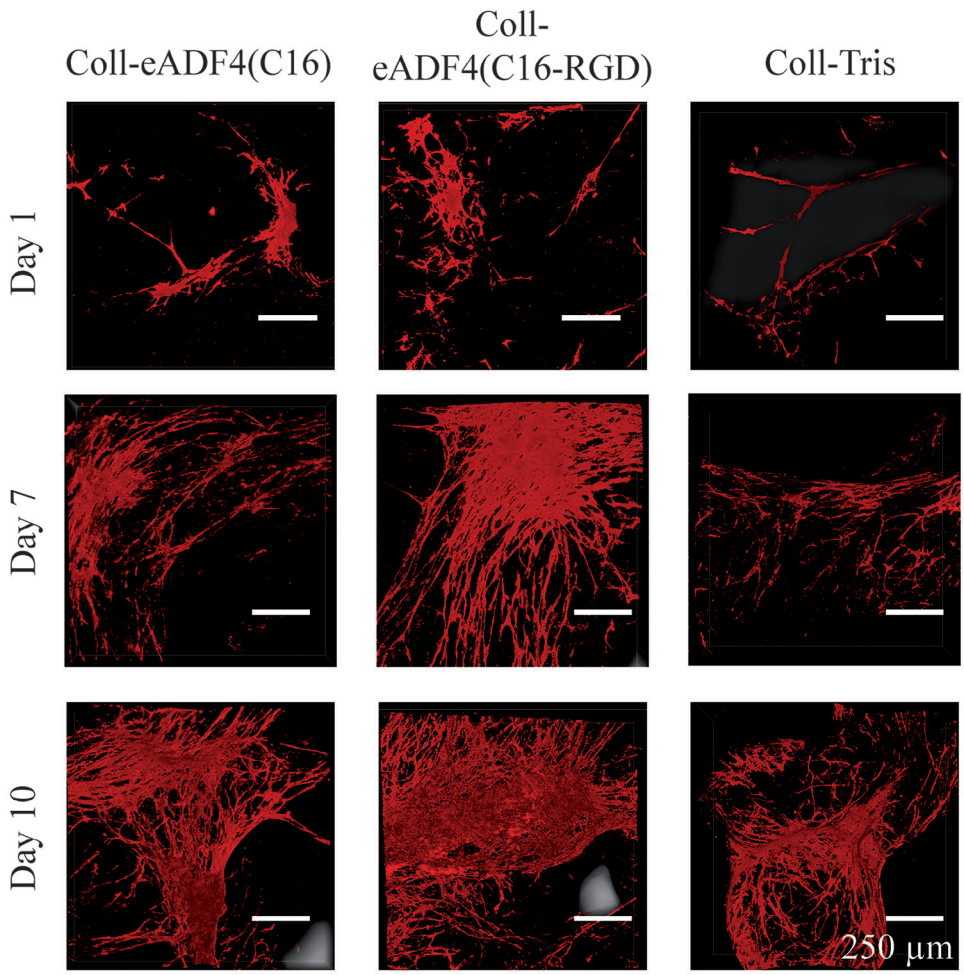


**Figure 7.** Confocal microscopy images of BJ morph fibroblasts (modified to express farnesylated tdTomato-protein, red) cultured on Coll-eADF4(C16), Coll-eADF4(C16-RGD), and Coll-Tris scaffolds after 1, 7, and 10 days ($n = 3$).

conditions, which is important to allow cells to attach and built up new extracellular matrix and regenerate tissue during wound healing. All scaffolds were stable in buffer, and a 7-day incubation did not result in hydrolysis or dissolution of the samples. This was confirmed by morphological analysis of the samples (Figure 6).

The intact, round Coll-eADF4(C16) scaffolds in TCNB buffer were recognizable until day 7. Based on the images, the disintegrated structure of the Coll-Tris samples was recognizable already on day 1, explaining the lower mechanical strength of the samples as well as the mechanical stress during washing or buffer exchange steps.

Since fibrillar collagens type I and III are the predominant components of the human skin ECM,[68] the collagen-silk composites as well as collagen-Tris scaffolds were examined in cell culture experiments with human skin fibroblasts (BJ Morph) and keratinocytes (HaCaT), the main cell types of dermis and epidermis,[69] respectively, to assess the biological functionality and cytocompatibility of the fabricated scaffolds. Fibroblast proliferation could be detected at 1, 4, 7, 10, and 14 days using confocal laser scanning microscopy (CLSM) since the BJ Morph cells continuously expressed a tomato-red gene visualizing the cell body (**Figure 7**).

Initially, the cells were distributed on the scaffolds along the struts and showed a characteristic, elongated morphology on all three samples. After 7 days, large areas of the scaffolds were covered by cells. When comparing the individual samples, no difference was apparent between the collagen-eADF4(C16) and collagen-eADF4(C16-RGD) scaffolds (Figure 7). Only on the pure collagen scaffolds (Coll-Tris) fewer cells were visible at the beginning due to the looser structure and the associated more difficult cell colonization. As the Coll-Tris scaffolds did not have to be moved for cell culture, cell seeding on the samples was possible in contrast to the mechanical testing, where the scaffolds had to be removed from the petri dish, which led to the collapse of the Coll-Tris-scaffolds. For additional visualization of the cell nuclei and the focal adhesion protein vinculin, further immunofluorescence staining and CLSM was performed on day 7. **Figure 8** shows the farnesylated tdTomato-protein (red), the cell nuclei (blue), and the focal adhesion protein vinculin (green) staining of fibroblasts on all three scaffolds.

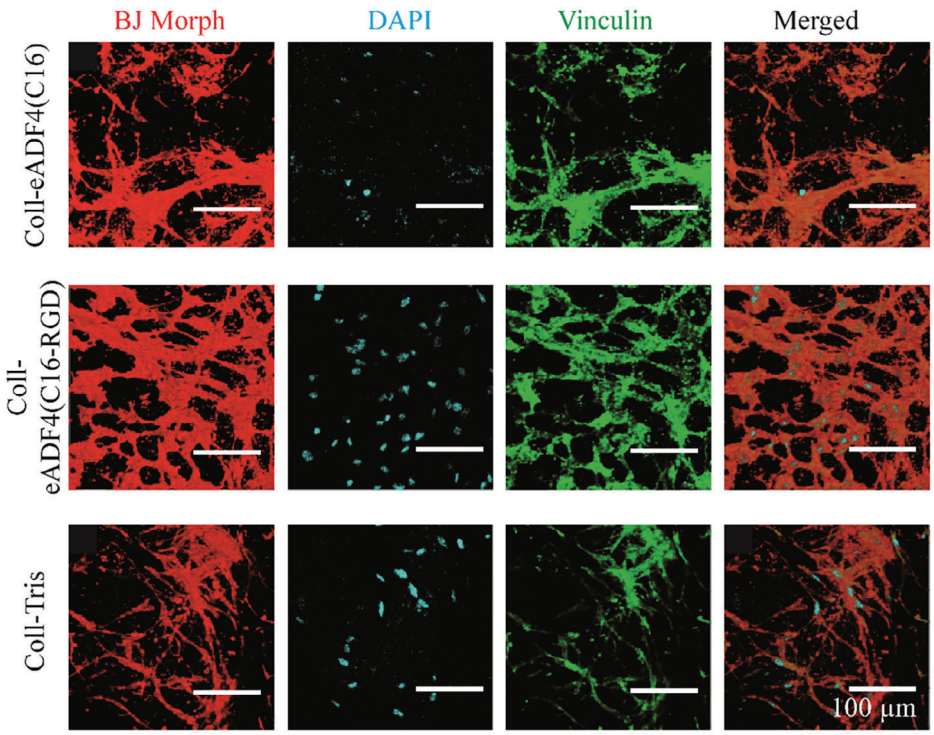


**Figure 8.** Representative confocal microscopy images of BJ Morph fibroblasts (farnesylated tdTomato-protein, red), nuclei (DAPI, blue), focal adhesion protein vinculin (TRITC-conjugated Phalloidin, green) and superimposed channels (merged) on coll-eADF4(C16), coll-eADF4(C16-RGD), and coll-Tris scaffolds after 7 days in culture ($n = 3$).

When comparing the collagen-spider silk scaffolds with and without RGD modification, no difference in cell density was observed, but the plain collagen scaffolds (Coll-Tris) showed again lower cell numbers. However, the high vinculin expression revealed a strong attachment of fibroblasts on all scaffolds. On day 10, the BJ cell number was increased on all scaffolds, and after 14 days a confluent cell layer was formed. In addition to fluorescence images, the interaction of the cells with the surrounding scaffold was considered using SEM to analyze cell interdependency with scaffold topography and possible cellular anchoring points (Figure S3, Supporting Information). SEM analysis indicated that fibroblasts not only adhered to the scaffold surfaces but also migrated into the interstices of the fibrils. Cells were located both above and below the collagen fibrils and spider silk particles. This was particularly evident with the lower cell number on day 1 (Figure S3A–C, Supporting Information). In addition, the cells spread along the collagen fibrils. Significantly larger cell numbers were observed on days 7 and 14. These results and findings confirmed the importance of the interplay of biochemical, mechanical, and topographical stimulation by a scaffold on successful cell attachment and proliferation.[53,70] In this context, the biological activity was mainly provided by cell interaction sites of collagen (e.g., DGEA, GFOGER, GLOGEN),[71] since no significant difference in cell numbers was detectable in presence of eADF4(C16) or eADF4(C16)-RGD. Thus, the RGD-tags were apparently not mandatory for supporting and improving cell interaction. However, the mechanically more stable, RGD-modified spider silk particles were very important to increase the mechanical and dimensional stability as well as shape fidelity of the 3D-bioprinted composite scaffolds. Here, the presence of additional RGD-peptides clearly increased the compressive stresses and compressive moduli of 3D-bioprinted collagen-spider silk scaffolds in comparison to particles made ot the non-modified eADF4(C16) spider silk.

After 14 days in culture, the collagen-spider silk as well as the collagen-Tris scaffolds showed a complete cell layer of fibroblasts (**Figure** 9B). The cells were cultured for another 7 days followed by a co-culture with human skin keratinocytes (HaCaTs) to develop a two-layer cell culture model (Figure 9). HaCaT keratinocytes were labeled with SYTO green fluorescent nucleic acid stain, seeded onto the fibroblast layer of the collagen-spider silk scaffolds, and cultured for additional 8 days. The coll-eADF4(C16) and coll-eADF4(C16-RGD) scaffolds showed complete BJ Morph fibroblast (red) and HaCaT keratinocyte (green) layers after 8 days of co-culture (Figure 9C). Due to the loose and fibrous structure and low mechanical stability of the Coll-Tris samples, no co-cultivation could be performed in this case. Taken together, our first cell culture experiments demonstrated that the 3D-bioprinted collagen-spider silk composite scaffolds displayed sufficient mechanical stability to provide a good environment for skin cells (fibroblasts, keratinocytes) and, thus, could enable skin tissue engineering in the future.

## 3. Conclusion and Outlook

In summary, the combination of collagen and recombinant eADF4(C16)-based spider silk proteins in one 3D printing process is a promising approach to fabricate dimensionally stable

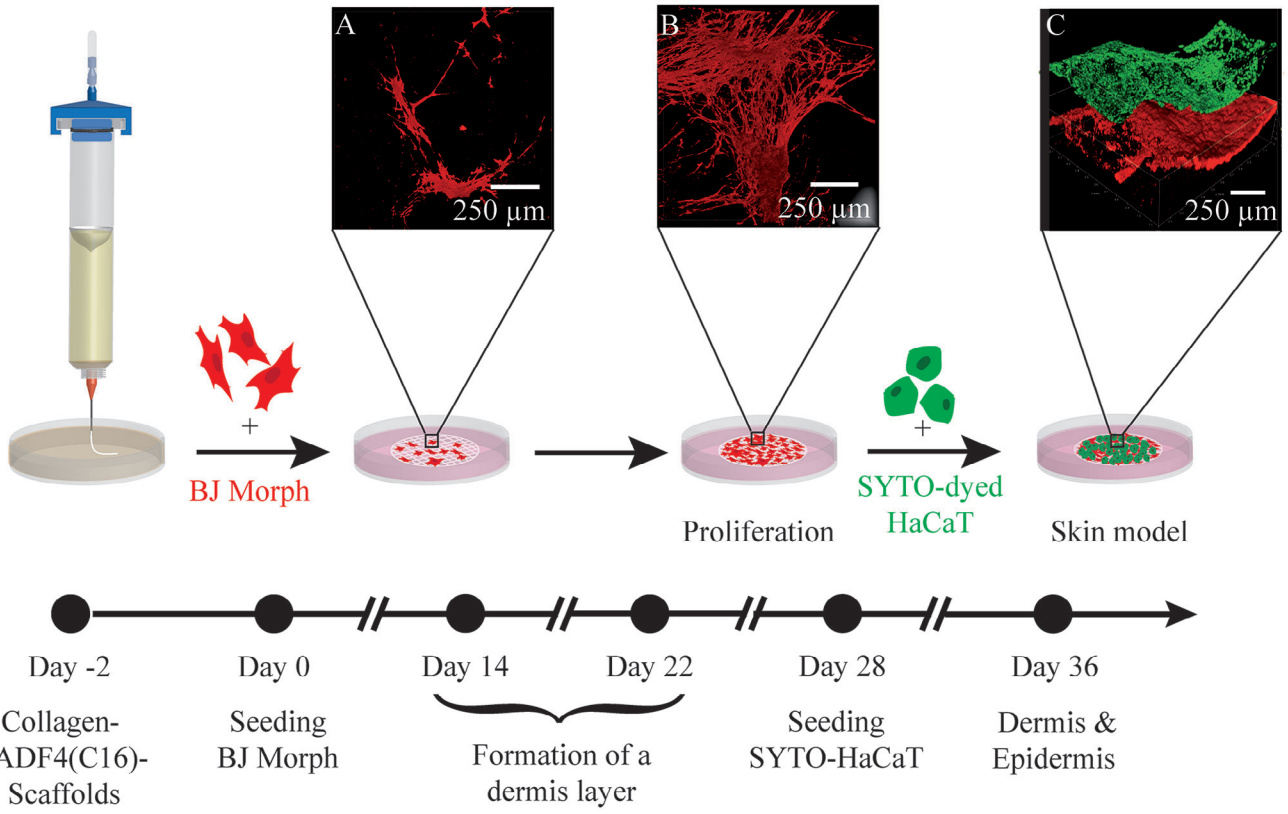


**Figure 9.** Schematic representation of cell culture experiments to fabricate a two-layer cell culture model consisting of human skin fibroblasts (BJ Morph, red) and keratinocytes (HaCaT, SYTO-dyed, green) seeded on 3D-printed collagen-spider silk composite scaffolds. Representative confocal microscopy images of fibroblasts after (A) seeding, (B) 14 days of cultivation and (C) co-cultivation using keratinocytes after 36 days.

composite scaffolds with high shape fidelity and adjustable mechanical properties for tissue regeneration. We established a novel and innovative 3D-bioprinting process for fibrillar collagens to overcome existing limitations such as phase separation of the bioink or low shape fidelity and insufficient mechanical stability of the construct. On the one hand, it is possible to use highly viscous, acidic collagen bioinks, since the physiological pH of the (spider silk) precipitation bath subsequently led to slow self-assembly of fibrillar collagen structures, and thus, to solidification of the 3D-printed scaffold. On the other hand, the precipitation of the spider silk particles between the collagen fibrils yielded 3D-printed collagen-spider silk composite scaffolds with increased shape accuracy and construct stability as well as adoptable mechanical properties. Thus, the presented two-step processing route combines the specific properties of the structural proteins collagen and spider silk in such a way that the unique functional, structural, and mechanical features of the individual biopolymers enable the formation of composite scaffolds with desired characteristics. Besides the enhanced mechanical stability, the spider silk particle reinforcement also led to increased proteolytic stability and slow biodegradation of the collagen scaffolds under wound-like conditions.

The fabricated collagen-spider silk composite scaffolds are biocompatible and contain bioactive cell interaction sites. In conclusion, the new 3D-bioprinting process allows the generation of particle reinforced collagen-spider silk composite scaffolds combining adjustable mechanical properties, slow biodegradation and biological activity to provide cells the necessary stability during tissue regeneration.

In the future, it is also possible to introduce more function into the composite scaffolds by using further modified spider silk proteins, for the coagulation bath.[72–74] For instance, since Neubauer et al. developed spider silk fusion proteins showing enhanced collagen interaction and biomineralization behavior, scaffolds for bone tissue engineering could also be fabricated by our 3D-printing process.[73] Since the coagulation bath has physiological conditions, it is further possible to adapt its components to incorporate living cells for encapsulating them inside the constructs. Furthermore, the biological activity of the presented system could be enriched by loading biologically active agents or drugs into the recombinant spider silk particles as previously shown.[39,49,74,75] Lastly, the ability of the 3D-bioprinted collagen-spider silk composites for clinical use as tissue engineering scaffolds should be evaluated in further studies.

## 4. Experimental Section

*Materials*: Collagen I/III grist from equine deep flexor tendon was provided by RESORBA (Nuremberg, Germany). Recombinant eADF4(C16) spider silk powder was purchased from AMSilk GmbH (Munich, Germany). Dulbecco's Modified Eagle's Medium (DMEM) and fetal calf

serum (FCS) were purchased from BioSell (Germany). Eagle's minimum essential medium (EMEM) and gentamycin sulfate were purchased from Sigma–Aldrich (Germany). Ethanol, hydrochloric acid (HCl), and phosphate-buffered saline (PBS) were obtained from VWR (Darmstadt, Germany). 4′,6-diamidino-2-phenylindole dihydrochloride (DAPI), the focal adhesion staining kit, GlutaMax (Gibco), dialysis membranes (Spectra/Por), and treated, as well as non-adherent well plates were obtained from Thermo Fisher Scientific (Bonn, Germany). All other chemicals were purchased from Carl-Roth GmbH + Co KG (Karlsruhe, Germany).

*Rheological Tests*: The rheological investigation of the collagen solutions was analyzed using a shear rheometer (Discovery HR-2 TA Instruments, Eschborn, Germany) in rotation mode with a 25 mm steel plate geometry and a gap size of 100 µm. The flow behavior was carried out by means of ramp tests with a shear rate range of 1–1000 1 $s^{-1}$ and a measuring time of 4 min at 25 °C. Ramp tests were carried out to investigate the printing solutions. The measurements were repeated on three individual samples from each test group.

*Preparation of Printing Solutions*: Collagen I/III grist was dissolved in 10 mM HCl at a concentration of 15 mg $mL^{-1}$ to achieve homogeneous solutions. The mixture was shaken vigorously until no pieces were visible, and mixing was continued for two days at 4 °C. Next, it was filtered through a membrane (90 × 90 µm mesh size) and centrifuged at 10 000 g for 10 min to remove air bubbles.

Recombinant eADF4(C16)-RGD spider silk protein was recombinantly produced and purified as described previously.[60,76] The freeze-dried spider silk proteins were dissolved in 6 M guanidinium thiocyanate at concentrations between 10 and 20 mg $mL^{-1}$ and dialyzed against 10 mM Tris/HCl buffer (pH 7.5) using membranes with a molecular weight cut-off of 6–8 kDa. Afterward, spider silk solutions were dialyzed against 25% (w/v) polyethylene glycol to increase the protein concentration as previously described.[67] The protein solutions were centrifuged (13 300 rpm, 10 min) to remove protein aggregates. For the analysis of the scaffold microstructure, eADF4(C16) was modified with rhodamine using a chemical covalent coupling as described previously.[77]

*3D-Printing and Scaffold Fabrication*: Collagen solutions were extruded into a coagulation bath consisting of aqueous spider silk solutions at concentrations of 20, 30, 40, and 50 mg $mL^{-1}$ using a 3D Discovery printer (regenHU, Villaz-St-Pierre, Swiss) with a feed rate of 5 mm $s^{-1}$. Pneumatic print heads were equipped with 3cc cartridge, pistons, and a 25G steel needle with an inner diameter of 260 µm (drifton, Denmark). The printing pressure was adjusted manually for optimal printing results (0.8–1.4 bar). Collagen solution printing in 10 mM Tris/HCl-buffer was used as a control. Printed constructs were incubated for 2 h in coagulation baths (spider silk solutions and Tris-buffer) at RT. Afterward, the bath solution was removed and exchanged using 1 M KPi (pH 7.5). The scaffolds were incubated overnight in a cell culture incubator (95% humidity) at 37 °C.

*Analysis of the Scaffold Microstructure*: The microstructure of the individual protein components and their interaction were studied using a rhodamine-labeled eADF4(C16) solution as a precipitation bath. For this purpose, 15 mg $mL^{-1}$ collagen solution was printed into a precipitation bath (20 mg $mL^{-1}$) containing 100% (v/v) unlabeled, 10% (v/v) Rhodamine-labeled and 100% (v/v) Rhodamine-labeled eADF4(C16). Samples were analyzed afterward using light and fluorescence microscopy, as well as scanning electron microscopy (SEM, Carl Zeiss Microscopy GmbH, Germany and Apreo VS, Thermo Fisher Scientific, Germany). For the latter, the samples were dehydrated using a gradual concentration of ethanol (50, 70, 80, 90, and 100% ethanol in water). Each step was conducted for 30 min, except the last step that was conducted overnight until ethanol was completely evaporated. Afterward, samples were treated with pure tert-butanol for 5 min at RT. Samples were frozen at –80 °C for 1 h before lyophilization overnight. Before imaging using SEM, samples were sputter-coated for 30 s at 30 mA with 2 nm platinum and imaged subsequently. Experiments were performed in triplicates.

*Assembly Kinetics*: To simulate the collagen-spider silk scaffold fabrication process, 100 µL of collagen solution was added to a 96-well plate, and 100 µL of eADF4(C16) (pH 7.5), eADF4(C16-RGD) (pH 7.5), or Tris buffer (pH 7.5) each, was added. The turbidity was measured at 570 nm. After 2 h, the turbidity measurement was interrupted, 1 M KPi buffer was added per 100 µL, and the measurement was continued for 16 h using an automated plate reader system (SpectraMax iD5, Molecular Devices). Experiments were performed in triplicates.

*Mechanical Properties*: To determine the mechanical properties of the collagen-silk scaffolds, circular models (diameter of 10 mm, height of 1.5 mm) were printed and stored in PBS buffer. The hydrated scaffolds were subjected to oscillatory compression tests (amplitude tests) at RT using DMA. At least 9 scaffolds were compressed from 1.3% to a maximum of 20% and back to 1.3% in 1.3% increments with a maximum force of 0.1 N and a frequency of 1 Hz at a pre-force of 1 N. The compression test was performed on 8 samples at a frequency of 1 Hz. Stress-compression curves (hysteresis curves) were determined using the recorded force-deformation data from the STARe software V16.40 (Mettler-Toledo GmbH). The curve fitting and determination of the mechanical characteristics compressive stress, compression, and Young's modulus were performed using Origin software (nonlinear function of a cubic polynomial, 3rd degree).

*Scaffold Degradation*: The proteolytic stability of 3D-printed collagen-eADF4(C16) and collagen-Tris scaffolds was analyzed under wound-like and digestive model conditions via in vitro enzymatic degradation following Müller-Herrmann et al.[66] For this purpose, circular morphologies with a diameter of 10 mm and a height of 1.5 mm, were printed, post-treated, and fixed on filter membranes (polyamide monofilament, web width 80 µm) using CellCrowns. Scaffolds were first sterilized in 70% ethanol for 30 min and then washed with TCNB buffer (50 mM Tris, 10 mM $CaCl_2$, 150 mM NaCl, and 0.05% (v/v) Brij, pH 7.5). In vitro degradation was analyzed based on protein release. Four scaffolds each were incubated in protease mixture PXIV (175 µg $mL^{-1}$ in TCNB buffer) from *Streptomyces griseus*, which resembles digestion conditions, and collagenase CHC (175 µg $mL^{-1}$ in TCNB buffer) from *Clostridium histolyticum* to simulate wound-like conditions. The protease mixture PXIV contained at least three caseinolytic activities plus an aminopeptidase activity and contained the following enzymes: *Streptomyces griseus* protease A, *Streptomyces griseus* protease B, and *Streptomyces griseus* trypsin. TCNB buffer was used as a control. The degradation was performed under physiological conditions in an incubator (37 °C, 10% $CO_2$, 95% humidity) over a period of 7 days. One milliliter of each enzyme mix or buffer solution was exchanged every 24 h. The supernatants were analyzed using UV–vis spectroscopy to evaluate the scaffold degradation. Experiments were performed in quadruplicate.

*Cell Culture Experiments*: Human BJ Morph fibroblasts were kindly provided by Lena Fischer and Dr. Ingo Thievessen (Biphysics group, University Erlangen-Nuremburg, Germany). BJ Morph fibroblasts were cultured in Eagle's minimum essential medium (EMEM) supplemented with 10% (v/v) FCS, 1% (v/v) GlutaMax, and 0.1% (v/v) gentamycin sulphate. Human HaCaT keratinocytes (DKFZ, CLS, Germany) were cultured in DMEM supplemented with 10% (v/v) FCS, 1% (v/v) GlutaMax, and 0.1% (v/v) gentamycin sulphate. Both cell lines were cultured in a cell culture incubator (HeraCell, Thermo Fisher Scientific) at humidified conditions containing 5% $CO_2$ at 37 °C. Subculturing was conducted using trypsin/Ethylenediaminetetraacetic acid. Cell numbers and viability were evaluated using trypan blue and an automated cell counter (TC20, Bio-Rad Laboratories, Germany). To analyze the cytocompatibility and adhesion behavior on 3D printed constructs, 60 000 BJ Morph fibroblasts were seeded onto each scaffold. The samples were incubated over 14 days and analyzed regarding cell proliferation.

For co-culture, HaCaT keratinocytes were stained using Syto 9 DNA stain (green, Invitrogen, Thermo Fisher Scientific) to allow a specific identification of keratinocytes (green) and BJ Morph (red) using fluorescence microscopy. Therefore, HaCaT keratinocytes were incubated with 1 µM Syto 9 DNA stain in DMEM for 1 h at 37 °C. Afterward, the cells were washed several times using 1xPBS to remove unspecifically surface bound dye. Keratinocytes were resuspended in DMEM/EMEM (1:1), and 50 000 cells were seeded on each scaffold (Coll-Tris, Coll-eADF4(C16), Coll-eADF4(C16)-RGD) containing confluent BJ-layers (cultured for 21 days).

*Analysis of Cell Proliferation, Morphology, and Viability*: Cell proliferation of BJ Morph fibroblasts and Syto 9-stained HaCaT keratinocytes on 3D-printed constructs were analyzed using a Leica DMI 8 confocal laser scanning microscope and the associated LAS X software (both Leica,

Germany). For focal adhesion staining, the samples were fixed using 4% (v/v) paraformaldehyde in 1xPBS and permeabilized using 0.1% (v/v) triton-X in 1xPBS. Samples were blocked using bovine serum albumine (BSA) solution. Cell nuclei were stained using DAPI (1:1000). Vinculin was stained using Anti-Vinculin (1:1000 in 1% BSA solution) for 1 h at RT. After several washing steps samples were incubated in secondary antibody Tetramethylrhodamin B isothiocyanate (TRITC)-conjugated Phalloidin (1:1000) solution. The same samples were also used to analyze the morphology of the cells and constructs using SEM. Viability of fibroblasts was evaluated in the collagen-silk composites fibers after 3 and 17 days of culture using 2 µM calcein acetomethylester (calcein) and visualized using a Leica DMI 8 confocal laser scanning microscope (Leica, Germany). Experiments were performed in triplicates.

*Statistical Analysis*: All measurements were made at least in triplicates. Data were reported as mean values ± standard deviation. The curve fitting and determination of the mechanical parameters compressive stress, compression, and modulus of elasticity were obtained by DMA carried out using Origin software (non-linear function of a cubic polynomial, 3rd degree).

## Supporting Information

Supporting Information is available from the Wiley Online Library or from the author.

## Acknowledgements

The authors would like to thank RESORBA for providing collagen grist I/III. The authors further want to acknowledge Lena Fischer and Dr. Ingo Thievessen for providing the BJ Morph reporter cell line. V.T.T. and T.S. acknowledge the Deutsche Forschungsgemeinschaft (DFG, German Research Foundation) project number 326998133-TRR225 funded subprojects A08 and C01 (T.S.). V.T.T. also acknowledges support from the Elite Network of Bavaria. The authors further thank Sahar Salehi for SEM imaging. The Elitenetzwerk Bayern to Vanessa TRossmann (fellowship).

Open access funding enabled and organized by Projekt DEAL.

## Conflict of Interest

T.S. is co-founder and shareholder of the company AMSilk GmbH.

## Author Contributions

K.S.K. and V.T.T. contributed equally to this work and are co-first authors. K.S.K, V.T.T., and T.S. conceptualized the study. K.S.K. and V.T.T. carried out the experimental work and analyzed the data. K.S.K and V.T.T. wrote and T.S. edited the original draft of the manuscript. T.S. acquired funding and supervised the study. All authors approved the final version of the manuscript.

## Data Availability Statement

The data that support the findings of this study are available from the corresponding author upon reasonable request.

## Keywords

collagen-silk-composites, nanofibrils, protein–protein-interactions, self-assembly

Received: May 7, 2024
Revised: July 8, 2024
Published online: July 27, 2024

[1] E. Osidak, P. Karalkin, M. S. Osidak, V. A. Parfenov, D. Sivogrivov, S. Domogatsky, *J. Mater. Sci.: Mater. Med.* **2019**, *30*, 31.
[2] S. Rhee, J. L. Puetzer, B. N. Mason, C. A. Reinhart-King, L. J. Bonassar, *ACS Biomater. Sci. Eng.* **2016**, *2*, 1800.
[3] W. W. Chan, D. C. L. Yeo, V. Tan, S. Singh, D. Choudhury, M. W. Naing, *Bioengineering.* **2020**, *7*, 66.
[4] a) D. Bagley, B. Bagley, D. Peterson, *WO2018/071639 ADVANCED BIOMATRIX, INC.* **2019**; b) A. K. Ralf Malessa, *JP2012140423A, Health Care AG*, **2011**.
[5] K. Tomihata, K. Burczak, K. Shiraki, Y. Ikada, *ACS Publications.* **1993**, *540*, 275.
[6] L. M. Delgado, Y. Bayon, A. Pandit, D. I. Zeugolis, *Tissue Eng., Part B.* **2015**, *21*, 298.
[7] a) X. Feng, P. Xu, T. Shen, Y. Zhang, J. Ye, C. Gao, *J. Mater. Chem. B.* **2020**, *8*, 391; b) S. Konar, P. Edwina, V. Ramanujam, A. Arunachalakasi, S. K. Bajpai, *J. Biomed. Mater. Res., Part B.* **2020**, *108*, 2368; c) F. G. Omenetto, D. L. Kaplan, H. Tao, B. Marelli, M. Yang, US 10,731,046 B2 Tufts University, **2018**.
[8] A. C. Heidenreich, M. Pérez-Recalde, A. González Wusener, É. B. Hermida, *Polym. Test.* **2020**, *82*, 106297.
[9] X. Yang, Z. Lu, H. Wu, W. Li, L. Zheng, J. Zhao, *Mater. Sci. Eng., C.* **2018**, *83*, 195.
[10] A. Mazzocchi, M. Devarasetty, R. Huntwork, S. Soker, A. Skardal, *Biofabrication.* **2018**, *11*, 015003.
[11] K.-F. Lin, S. He, Y. Song, C.-M. Wang, Y. Gao, J.-Q. Li, P. Tang, Z. Wang, L. Bi, G.-X. Pei, *ACS Appl. Mater. Interfaces.* **2016**, *8*, 6905.
[12] a) R. Z. Wang, F. Z. Cui, H. B. Lu, H. B. Wen, C. L. Ma, H. D. Li, *J. Mater. Sci. Lett.* **1995**, *14*, 490; b) D. A. Wahl, J. T. Czernuszka, *Eur. Cells Mater.* **2006**, *11*, 43; c) D. A. Wahl, E. Sachlos, C. Liu, J. T. Czernuszka, *Mater. Med.* **2007**, *18*, 201.
[13] R. J. Kane, H. E. Weiss-Bilka, M. J. Meagher, Y. Liu, J. A. Gargac, G. L. Niebur, D. R. Wagner, R. K. Roeder, *Acta Biomater.* **2015**, *17*, 16.
[14] a) A. A. Al-Munajjed, F. J. O'Brien, *J. Mech. Behav. Biomed. Mater.* **2009**, *2*, 138; b) A. A. Al-Munajjed, N. A. Plunkett, J. P. Gleeson, T. Weber, C. Jungreuthmayer, T. Levingstone, J. Hammer, F. J. O'Brien, *J. Biomed. Mater. Res., Part B.* **2009**, *90*, 584.
[15] S. G. Patrício, L. R. Sousa, T. R. Correia, V. M. Gaspar, L. S. Pires, J. L. Luís, J. M. Oliveira, J. F. Mano, *Biofabrication.* **2020**, *12*, 035017.
[16] A. Lee, A. R. Hudson, D. J. Shiwarski, J. W. Tashman, T. J. Hinton, S. Yerneni, J. M. Bliley, P. G. Campbell, A. W. Feinberg, *Science.* **2019**, *365*, 482.
[17] a) M. A. Skylar-Scott, S. G. M. Uzel, L. L. Nam, J. H. Ahrens, R. L. Truby, S. Damaraju, J. A. Lewis, *Sci. Adv.* **2019**, *5*, eaaw2459; b) J. A. Lewis, K. A. Homan, D. B. Kolesky, R. L. Truby, M. A. S. Scott, US 10,702,630 B2 President and Fellows of Harvard College, **2020**.
[18] J. Sik (KR), M. Ahn, KR20180049745A, Pohang University of Science and Technology, **2016**.
[19] D. Steiner, G. Lang, L. Fischer, S. Winkler, T. Fey, P. Greil, T. Scheibel, R. E. Horch, A. Arkudas, *Tissue Eng., Part A.* **2019**, *25*, 1504.
[20] M. Beena, J. M. Ameer, N. Kasoju, *ACS Omega.* **2022**, *7*, 29634.
[21] F. Schäfer-Nolte, K. Hennecke, K. Reimers, R. Schnabel, C. Allmeling, P. M. Vogt, J. W. Kuhbier, U. Mirastschijski, *Ann. Surg.* **2014**, *259*, 781.
[22] F. Seijsing, L. Nilebäck, O. Öhman, R. Pasupuleti, C. Ståhl, J. Seijsing, M. Hedhammar, *MicrobiologyOpen.* **2020**, *9*, e993.
[23] L. Peng, H. Wang, G. Li, Z. Liang, W. Zhang, W. Zhao, T. An, *Nat. Commun.* **2023**, *14*, 2412.
[24] S. Kumari, G. Lang, E. DeSimone, C. Spengler, V. T. Trossmann, S. Lücker, M. Hudel, K. Jacobs, N. Krämer, T. Scheibel, *Mater. Today.* **2020**, *41*, 21.
[25] S. Zhang, D. Piorkowski, W.-R. Lin, Y.-R. Lee, C.-P. Liao, P.-H. Wang, I.-M. Tso, *J. Exp. Biol.* **2019**, *222*, jeb214981.

[26] S. Wright, S. L. Goodacre, *BMC Res. Notes.* **2012**, *5*, 326.
[27] S. Salehi, K. Koeck, T. Scheibel, *Molecules.* **2020**, *25*, 737.
[28] C. Holland, K. Numata, J. Rnjak-Kovacina, F. P. Seib, *Adv. Healthcare Mater.* **2019**, *8*, e1800465.
[29] C. Belbéoch, J. Lejeune, P. Vroman, F. Salaün, *Environ. Chem. Lett.* **2021**, *19*, 1737.
[30] C. N. Keiser, A. E. DeMarco, T. A. Shearer, J. A. Robertson, J. N. Pruitt, *J. Arachnol.* **2015**, *43*, 394.
[31] V. T. Trossmann, T. Scheibel, in *Silk-Based Biomaterials for Tissue Engineering, Regenerative and Precision Medicine*, Elsevier, Amsterdam/New York **2024**, pp. 133–190.
[32] V. T. Trossmann, S. Lentz, T. Scheibel, *J. Funct. Biomater.* **2023**, *14*, 434.
[33] P. H. Zeplin, N. C. Maksimovikj, M. C. Jordan, J. Nickel, G. Lang, A. H. Leimer, L. Römer, T. Scheibel, *Adv. Funct. Mater.* **2014**, *24*, 2658.
[34] S. Gomes, J. Gallego-Llamas, I. B. Leonor, J. F. Mano, R. L. Reis, D. L. Kaplan, *Macromol. Biosci.* **2013**, *13*, 444.
[35] L. Baoyong, Z. Jian, C. Denglong, L. Min, *Burns.* **2010**, *36*, 891.
[36] G. H. Altman, F. Diaz, C. Jakuba, T. Calabro, R. L. Horan, J. Chen, H. Lu, J. Richmond, D. L. Kaplan, *Biomaterials.* **2003**, *24*, 401.
[37] K. Gellynck, P. Verdonk, R. Forsyth, K. F. Almqvist, E. van Nimmen, T. Gheysens, J. Mertens, L. van Langenhove, P. Kiekens, G. Verbruggen, *J. Mater. Sci. Mater. Med.* **2008**, *19*, 2963.
[38] C. Liebsch, V. Bucan, B. Menger, F. Köhne, K.-H. Waldmann, D. Vaslaitis, P. M. Vogt, S. Strauss, J. W. Kuhbier, *Burns.* **2018**, *44*, 1829.
[39] D. Steiner, S. Winkler, S. Heltmann-Meyer, V. T. Trossmann, T. Fey, T. Scheibel, R. E. Horch, A. Arkudas, *Biofabrication.* **2021**, *13*, 045003.
[40] B. Bakhshandeh, S. S. Nateghi, M. M. Gazani, Z. Dehghani, F. Mohammadzadeh, *Int. J. Biol. Macromol.* **2021**, *192*, 258.
[41] M. Saric, T. Scheibel, *Curr. Opin. Biotechnol.* **2019**, *60*, 213.
[42] C. H. Bowen, B. Dai, C. J. Sargent, W. Bai, P. Ladiwala, H. Feng, W. Huang, D. L. Kaplan, J. M. Galazka, F. Zhang, *Biomacromolecules.* **2018**, *19*, 3853.
[43] D. M. d. C. Bittencourt, P. Oliveira, V. A. Michalczechen-Lacerda, G. M. S. Rosinha, J. A. Jones, E. L. Rech, *Front. Bioeng. Biotechnol.* **2022**, *10*, 958486.
[44] T. B. Aigner, E. DeSimone, T. Scheibel, *Adv. Mater.* **2018**, *30*, 1704636.
[45] A. Fallahi, I. K. Yazdi, L. Serex, E. Lesha, N. Faramarzi, F. Tarlan, H. Avci, R. Costa-Almeida, F. Sharifi, C. Rinoldi, M. E. Gomes, S. Ryon Shin, A. Khademhosseini, M. Akbari, A. Tamayol, *ACS Biomater. Sci. Eng.* **2020**, *6*, 1112.
[46] O. Shchepelina, I. Drachuk, M. K. Gupta, J. Lin, V. V. Tsukruk, *Adv. Mater.* **2011**, *23*, 4655.
[47] L. Gustafsson, C. P. Tasiopoulos, R. Jansson, M. Kvick, T. Duursma, T. C. Gasser, W. van der Wijngaart, M. Hedhammar, *Adv. Funct. Mater.* **2020**, *30*, 2002982.
[48] A. C. G. Weiss, H. M. Herold, S. Lentz, M. Faria, Q. A. Besford, C.-S. Ang, F. Caruso, T. Scheibel, *ACS Appl. Mater. Interfaces.* **2020**, *12*, 24635.
[49] A. Lammel, M. Schwab, M. Hofer, G. Winter, T. Scheibel, *Biomaterials.* **2011**, *32*, 2233.
[50] U. Johansson, M. Widhe, N. D. Shalaly, I. L. Arregui, L. Nilebäck, C. P. Tasiopoulos, C. Åstrand, P.-O. Berggren, C. Gasser, M. Hedhammar, *Sci. Rep.* **2019**, *9*, 6291.
[51] a) T. Arndt, U. Chatterjee, O. Shilkova, J. Francis, J. Lundkvist, D. Johansson, B. Schmuck, G. Greco, Å. E. Nordberg, Y. Li, L. U. Wahlberg, M. Langton, J. Johansson, C. Götherström, A. Rising, *Adv. Funct. Mater.* **2023**, 2303622; b) V. J. Neubauer, V. T. Trossmann, S. Jacobi, A. Döbl, T. Scheibel, *Angew. Chem.* **2021**, *60*, 11847.
[52] a) D. H. de Oliveira, V. Gowda, T. Sparrman, L. Gustafsson, R. Sanches Pires, C. Riekel, A. Barth, C. Lendel, M. Hedhammar, *Nat. Commun.* **2024**, *15*, 4670; b) B. Schmuck, G. Greco, T. B. Pessatti, S. Sonavane, V. Langwallner, T. Arndt, A. Rising, *Adv. Funct. Mater.* **2023**, 2305040.
[53] B. Bakhshandeh, N. Ranjbar, A. Abbasi, E. Amiri, A. Abedi, M.-R. Mehrabi, Z. Dehghani, C. P. Pennisi, *Bioeng. Transl. Med.* **2023**, *8*, e10383.
[54] a) X. Hu, P. Cebe, A. S. Weiss, F. Omenetto, D. L. Kaplan, *Mater. Today.* **2012**, *15*, 208; b) A. Sionkowska, *Prog. Polym. Sci.* **2011**, *36*, 1254.
[55] a) N. Johari, A. Khodaei, A. Samadikuchaksaraei, R. L. Reis, S. C. Kundu, L. Moroni, *Acta Biomater.* **2022**, *153*, 38; b) A. W. Morgan, K. E. Roskov, S. Lin-Gibson, D. L. Kaplan, M. L. Becker, C. G. Simon, *Biomaterials.* **2008**, *29*, 2556; c) C. Laomeephol, A. Vasuratna, J. Ratanavaraporn, S. Kanokpanont, J. A. Luckanagul, M. Humenik, T. Scheibel, S. Damrongsakkul, *Polymers.* **2021**, *13*, 4182; d) D. Bobylev, M. Wilhelmi, S. Lau, M. Klingenberg, M. Mlinaric, E. Petená, F. Helms, T. Hassel, A. Haverich, A. Horke, U. Böer, *J. Biomater. Appl.* **2022**, *36*, 1126.
[56] X. Peng, Y. Cui, J. Chen, C. Gao, Y. Yang, W. Yu, K. Rai, M. Zhang, R. Nian, Z. Bao, Y. Sun, *ACS Biomater. Sci. Eng.* **2022**, *8*, 3341.
[57] F. Schlottmann, S. Strauss, C. Plaass, B. Welke, P. M. Vogt, J. W. Kuhbier, *Appl. Sci.* **2021**, *11*, 1218.
[58] U. K. Slotta, S. Rammensee, S. Gorb, T. Scheibel, *Angew. Chem.* **2008**, *120*, 4668.
[59] A. Lammel, M. Schwab, U. Slotta, G. Winter, T. Scheibel, *ChemSusChem.* **2008**, *1*, 413.
[60] T. U. Esser, V. T. Trossmann, S. Lentz, F. B. Engel, T. Scheibel, *Mater. Today Bio.* **2021**, *11*, 100114.
[61] a) N. Yamamoto, *Eup. J. Biophys.* **2017**, *5*, 1; b) K. S. Koeck, S. Salehi, M. Humenik, T. Scheibel, *Adv. Funct. Mater.* **2022**, *32*, 2112238.
[62] K. Schacht, T. Scheibel, *Biomacromolecules.* **2011**, *12*, 2488.
[63] a) A. Lechner, V. T. Trossmann, T. Scheibel, *Macromol. Biosci.* **2021**, 2100390; b) K. Schacht, T. Jüngst, M. Schweinlin, A. Ewald, J. Groll, T. Scheibel, *Angew. Chem.* **2015**, *54*, 2816.
[64] J. Gao, C. Tang, M. A. Elsawy, A. M. Smith, A. F. Miller, A. Saiani, *Biomacromolecules.* **2017**, *18*, 826.
[65] S. P. Zustiak, R. Durbal, J. B. Leach, *Acta Biomater.* **2010**, *6*, 3404.
[66] S. Müller-Herrmann, T. Scheibel, *ACS Biomater. Sci. Eng.* **2015**, *1*, 247.
[67] S. Lentz, V. T. Trossmann, C. B. Borkner, V. Beyersdorfer, M. Rottmar, T. Scheibel, *ACS Appl. Mater. Interfaces.* **2022**, *14*, 31751.
[68] E. H. Epstein, N. H. Munderloh, *J. Biol. Chem.* **1978**, *253*, 1336.
[69] C. E. M. Griffiths, J. Barker, T. Bleiker, R. J. G. Chalmers, D. Creamer, *Rook's Textbook of Dermatology*, John Wiley & Sons Inc, Chichester, West Sussex, Hoboken, NJ **2016**.
[70] a) G. Huang, F. Li, X. Zhao, Y. Ma, Y. Li, M. Lin, G. Jin, T. J. Lu, G. M. Genin, F. Xu, *Chem. Rev.* **2017**, *117*, 12764; b) A.-S. Mertgen, V. T. Trossmann, A. G. Guex, K. Maniura-Weber, T. Scheibel, M. Rottmar, *ACS Appl. Mater. Interfaces.* **2020**, *12*, 21342; c) S. M. Dellatore, A. S. Garcia, W. M. Miller, *Curr. Opin. Biotechnol.* **2008**, *19*, 534.
[71] a) K. Sivaraman, K. Muthukumar, C. Shanthi, *Cell Biol. Int.* **2022**, *46*, 391; b) J. Heino, *BioEssays.* **2007**, *29*, 1001; c) C. G. Knight, L. F. Morton, A. R. Peachey, D. S. Tuckwell, R. W. Farndale, M. J. Barnes, *J. Biol. Chem.* **2000**, *275*, 35.
[72] V. T. Trossmann, T. Scheibel, *Adv. Healthcare Mater.* **2023**, *12*, e2202660.
[73] V. J. Neubauer, T. Scheibel, *ACS Biomater. Sci. Eng.* **2020**, *6*, 5599.
[74] M. B. Schierling, E. Doblhofer, T. Scheibel, *Biomater. Sci.* **2016**, *4*, 1515.
[75] a) S. Kumari, H. Bargel, M. U. Anby, D. Lafargue, T. Scheibel, *ACS Biomater. Sci. Eng.* **2018**, *4*, 1750; b) H. M. Herold, A. Döbl, S. Wohlrab, M. Humenik, T. Scheibel, *Biomacromolecules.* **2020**, *21*, 4904; c) E. Doblhofer, T. Scheibel, *J. Pharm. Sci.* **2015**, *104*, 988; d) K. Kucharczyk, M. Weiss, K. Jastrzebska, M. Luczak, A. Ptak, M. Kozak, A. Mackiewicz, H. Dams-Kozlowska, *Int. J. Nanomed.* **2018**, *13*, 4247; e) A. Florczak, A. Mackiewicz, H. Dams-Kozlowska,

*Biomacromolecules*. **2014**, *15*, 2971; f) K. Kucharczyk, A. Florczak, T. Deptuch, K. Penderecka, K. Jastrzebska, A. Mackiewicz, H. Dams-Kozlowska, *J. Nanobiotechnol*. **2020**, *18*, 56; g) A. Florczak, T. Deptuch, K. Kucharczyk, H. Dams-Kozlowska, *Cancers*. **2021**, *13*, 5389.

[76] S. Wohlrab, S. Müller, A. Schmidt, S. Neubauer, H. Kessler, A. Leal-Egaña, T. Scheibel, *Biomaterials*. **2012**, *33*, 6650.

[77] C. B. Borkner, S. Wohlrab, E. Möller, G. Lang, T. Scheibel, *ACS Biomater. Sci. Eng*. **2017**, *3*, 767.